JOURNAL OF SPACECRAFT AND ROCKETS
Vol. 47, No. 5, September–October 2010

Performance Characterization of Supersonic Retropropulsion for High-Mass Mars Entry Systems

Ashley M. Korzun* and Robert D. Braun†
Georgia Institute of Technology, Atlanta, Georgia 30332

DOI: 10.2514/1.49803

Prior high-mass Mars entry systems studies have neglected aerodynamic–propulsive interactions and subsequent performance impacts during the supersonic phase of descent. The goal of this investigation is to accurately evaluate the performance of supersonic retropropulsion as a function of vehicle ballistic coefficient and thrust available, defining a range of initiation conditions relevant for future high-mass Mars entry systems. Past experimental work has established trends in static aerodynamics for supersonic retropropulsion as a function of retropropulsion configuration, freestream conditions, and thrust. From this experimental database, an aerodynamic–propulsive interactions model is created. Entry system performance results are developed with the experimentally derived aerodynamic drag preservation models included and excluded during this phase of flight for comparison against prior studies. The results of this investigation demonstrate the significance of aerodynamic drag preservation as a function of retropropulsion initiation conditions and characterize optimal trajectories using supersonic retropropulsion.

Nomenclature

A	=	reference area, m^2
C	=	force coefficient
D	=	drag, N
g	=	gravitational acceleration, m/s^2
I_{sp}	=	specific impulse, s
L/D	=	hypersonic lift-to-drag ratio
m	=	mass, kg
p	=	pressure, Pa
q	=	dynamic pressure, Pa
$\dot{q}$	=	heat rate, W/cm^2
r	=	radius, m
T	=	thrust, N
T/W	=	vehicle thrust-to-weight ratio
t	=	time, s
V	=	volume, m^3
v	=	relative velocity, m/s
β	=	vehicle hypersonic ballistic coefficient, kg/m^2
γ	=	relative flight path angle, deg
ΔV	=	velocity increment, m/s
ρ	=	density, kg/m^3
ϕ	=	tank mass factor, m

Subscripts

A	=	axial
D	=	drag
f	=	forebody
n	=	nose
prop	=	propellant
req	=	required
T	=	thrust
∞	=	freestream

Presented as Paper 2009-5613 at the AIAA Atmospheric Flight Mechanics Conference, Chicago, IL, 10–13 August 2009; received 10 March 2010; revision received 21 June 2010; accepted for publication 21 June 2010.

*Graduate Research Assistant, Daniel Guggenheim School of Aerospace Engineering, 270 Ferst Drive. Student Member AIAA.

†Professor, Daniel Guggenheim School of Aerospace Engineering, 270 Ferst Drive. Fellow AIAA.

I. Introduction

TO DATE, the United States has successfully landed six robotic missions on Mars. Including missions planned for this decade, the largest entry mass sent to Mars will be Mars Science Laboratory (MSL) at ~3300 kg [1]. The entry, descent, and landing (EDL) systems for these missions rely heavily on extensions of Viking-heritage technology, namely supersonic disk-gap-band (DGB) parachutes and 70-deg sphere-cone, blunt body aeroshells. Supersonic deceleration has been identified as a critical deficiency in extending these heritage technologies to high-mass, high ballistic coefficient systems [1,2].

A key parameter used to describe an entry vehicle is the ballistic coefficient, β, or the ratio of entry mass to hypersonic vehicle drag area, defined in Eq. (1):

$$\beta = \frac{m_{\text{entry}}}{C_D A} \tag{1}$$

The six successful Mars landers have all had ballistic coefficients under 100 kg/m^2 [1]. Requirements for substantial (one or two orders of magnitude) increases in landed mass and aeroshell packaging constraints result in significantly higher ballistic coefficients for human-scale Mars entry systems (~400 kg/m^2 and higher) [1]. For these high ballistic coefficient vehicles, the thin Martian atmosphere and the challenge of extending supersonic DGB parachutes to the required dimensions and deployment conditions combine to severely reduce the timeline available for deceleration and transition from a hypersonic entry vehicle to a terminal landing configuration. System-level studies to assess the required performance of high-mass entry systems recommend the development of alternative supersonic decelerators, a challenge potentially addressed by supersonic retropropulsion (SRP) [1].

SRP is the initiation of a propulsive deceleration phase while the vehicle is traveling supersonically. The SRP flowfield is a complex interaction between a typically highly underexpanded jet and an opposing supersonic freestream. The aerodynamic characteristics of the vehicle are affected by both the thrust of the retropropulsion and by the interaction between the retropropulsion and the supersonic freestream [3]. The retropropulsion plumes obstruct the oncoming freestream, and a bow shock forms. The supersonic freestream flow is decelerated to subsonic by the bow shock, and the supersonic jet flow is decelerated to subsonic by a Mach disk (normal shock). A contact surface separates the subsonic retropropulsion flow and the subsonic freestream flow behind the bow shock. The shape of the contact surface acts as the effective vehicle geometry, or flow obstruction, seen by the supersonic freestream flow [3].

Results from wind tunnel experiments in the 1960s and early 1970s demonstrate the potential to preserve aerodynamic drag during a SRP phase for peripheral retropropulsion configurations at low-to-moderate thrust levels [4]. The degree of aerodynamic drag preservation is strongly dependent upon the location of the nozzles on the vehicle forebody and the relative strength of the exhaust flow to the freestream, both of which determine the shape of the contact surface [3,5–9]. Aerodynamic drag preservation is possible for configurations and conditions for which the bow shock remains undisturbed by the retropropulsion flow and high surface pressures are maintained [3]. In contrast, little or no preservation of aerodynamic drag has been experimentally observed for configurations that thrust through the nose along the body centerline. Generally, directing thrust along the body centerline forms a contact surface that is more oblique than the body, contributing to a reduction in surface pressure as compared with the body with no SRP. Aerodynamic drag is not preserved when the freestream flow is unable to reach the body [3]. The static aerodynamics resulting from the aerodynamic–propulsive interaction are a strong function of thrust coefficient, C_T [defined in Eq. (2)], with the greatest degree of aerodynamic drag preservation occurring for peripheral retropropulsion configurations with $C_T < 1$. In the context of SRP system performance, C_T is a force coefficient and is not a direct function of the nozzle geometry:

$$C_T = \frac{T}{q_\infty A} \tag{2}$$

Past experimental work has demonstrated SRP on a small scale, establishing trends in static aerodynamics as a function of retropropulsion configuration, freestream conditions, and thrust [4]. However, most prior high-mass Mars EDL systems studies [1,2,10] have neglected aerodynamic–propulsive interactions and the associated performance impacts during the supersonic phase of descent. This investigation addresses the applicability, limitations, and performance implications of SRP technology in the context of future human and robotic Mars exploration missions. The goals of this investigation are to characterize the performance of SRP with increasing vehicle ballistic coefficient and to define a range of relevant initiation conditions. The maximum allowable vehicle T/W is determined through multi-objective optimization to minimize both the total mass and total volume required for the propulsion system. Results are presented with the potential aerodynamic drag preservation included and excluded during the SRP phase for comparison against prior studies. The results of this investigation demonstrate the significance of aerodynamic drag preservation as a function of retropropulsion initiation conditions and characterize optimal trajectories utilizing SRP. Additional treatment is given to the accuracy of SRP modeling assumptions in the context of experimentally observed trends for drag preservation and the sensitivity of the results of this study to I_{sp}. A sample robotic-scale case is presented for comparison with the human-scale cases considered in this study.

II. Approach

The hypersonic and supersonic phases of a Mars entry trajectory are modeled and simulated. SRP is utilized to decelerate the vehicle to the desired terminal state. The analysis is performed as a single-objective optimization problem. Vehicle ballistic coefficients of 200, 400, and 600 kg/m^2 are considered for the human-scale cases, and an MSL-derived case ($\beta = 185$ kg/m^2, 4.5 m-diam 70-deg sphere-cone aeroshell) is considered for extension to future robotic-scale missions. All cases are constrained by the same initial and final altitude and velocity conditions (those at the atmospheric interface and retropropulsion termination).

A. Analysis Methods

The three-dimensional translational equations of motion are integrated from a specified set of initiation conditions (altitude, mass, and velocity) to minimize the ΔV required from the propulsion system and to simultaneously target Mach 0.9 and 3 km altitude, the chosen subsonic terminal conditions. These terminal conditions are considered to be conservative with respect to available timeline and mission constraints. The Program to Optimize Simulated Trajectories, known as POST II [11], is used to model and simulate both the hypersonic lifting entry phase and ballistic SRP phase. Optimization and targeting use 17 design variables (relative entry flight path angle, 7 bank angle settings, the time of SRP initiation, and eight throttle settings) to satisfy an objective to maximize final vehicle mass.

Gravity, thrust, and aerodynamic drag forces are modeled over the trajectory, with thrust modeled from a throttle profile as a function of relative velocity. Relative velocity was chosen to provide adequate resolution within the thrust profile across the conditions of interest for each case. Aerodynamic force coefficients are interpolated between tabulated points as a function of Mach number (hypersonically) and Mach number and thrust coefficient (supersonically). A nominal tabulated atmosphere (−2.5 km to 128 km) based on a reconstructed Mars Pathfinder entry mission scenario is used for all density, pressure, and temperature values as functions of altitude [12]. Mars and its atmosphere were assumed to rotate with constant angular velocity. All cases assume a direct entry, with a relative velocity at the atmospheric interface of 5400 m/s.

B. Vehicle Configuration

The vehicle is assumed to be a 70-deg sphere-cone with three axially-aligned, bipropellant engines at the periphery of the forebody. Past work by Christian et al. [2] showed that for a blunt entry body, a propulsive configuration with the engines towards the forebody periphery provides more useful volume for payload and propellant tanks than a cluster of engines at the center. This configuration is also consistent with the peripheral configuration used to develop the aerodynamic–propulsive interactions model (see Sec. II.C). An example of a peripheral retropropulsion configuration is given in Fig. 1, and the aeroshell geometry is given in Fig. 2. The total volume of this 10 m-diam aeroshell is 247.2 m^3.

Table 1 gives approximate entry masses corresponding to the ballistic coefficients used in this investigation for 10 m-diam, 70-deg sphere-cone aeroshells. This entry mass range is consistent with those assumed in NASA Design Reference Architecture 5.0 [10] and other studies of future human Mars exploration systems [2,4,13–15].

C. Aerodynamic–Propulsive Interactions Model (SRP)

The aerodynamic–propulsive interactions model used during the SRP phase is based on experimental work by Jarvinen and Adams [5] for a peripheral retropropulsion configuration similar to the one shown in Fig. 1. The experimental data used to construct the model, as well as a comparison between peripheral and central retropropulsion configurations, are given in Fig. 3. All experimental data

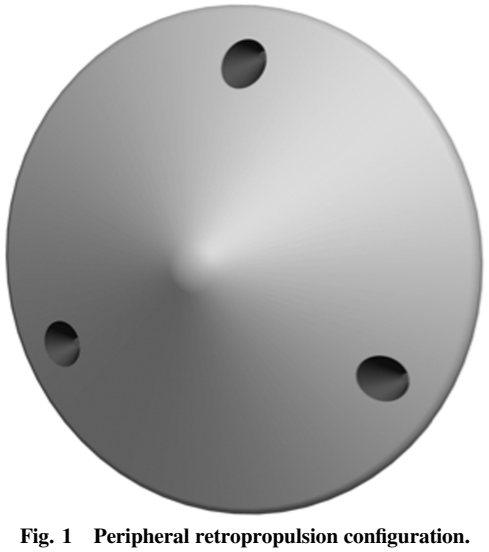

Fig. 1 Peripheral retropropulsion configuration.

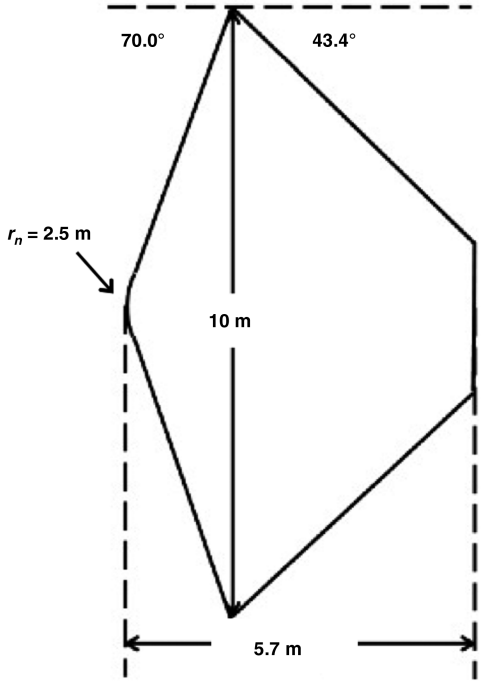

Fig. 2 70-deg sphere-cone aeroshell geometry.

shown are for zero angle of attack; C_A is equivalent to the sum of C_D and C_T for such conditions.

For a given vehicle T/W and real-time trajectory conditions, the aerodynamic–propulsive interactions model is referenced to determine the total axial force. While the current form of the model does not include variations with Mach number, McGhee [7], with Jarvinen and Adams [5] and Keyes and Hefner [9], observed only minor variations in axial force coefficient with C_T across initiation Mach numbers of 2.0 to 6.0 (see Fig. 3). The trajectory conditions require a deceleration force greater than the aerodynamic drag provided by the blunt body for the model to be active. For thrust coefficients above 3.0, the deceleration force coefficient ($C_{A,\text{total}}$) is equivalent to the thrust coefficient, and no aerodynamic contribution to the deceleration is applied. Figure 4 illustrates the multiplier applied to the supersonic C_D as a function of C_T for both a peripheral and a central retropropulsion configuration. The sharp slope changes in Fig. 4 are a result of the limited data available to construct the model.

D. Determination of Vehicle $(T/W)_{\max}$

The results of this investigation, specifically the range of SRP initiation and operating conditions, are dependent on the maximum allowable system T/W. SRP initiation occurs at conditions that maximize final vehicle mass, effectively minimizing the required propulsive ΔV; the required propulsive ΔV is a direct function of the thrust available. For each ballistic coefficient (200, 400, 600 kg/m^2), the selection of $(T/W)_{\max}$ is considered as a multi-objective optimization problem. The two objectives are 1) to minimize total propulsion system mass (engines, tanks, and propellant) and 2) to minimize the total volume required for the propulsion system. Plotting these two objectives against one another for a range of $(T/W)_{\max}$ yields a collection of Pareto-optimal points, or points for which improvement in one objective leads to degradation in the other

Table 1 Entry masses (kg) for a 10 m-diam, 70-deg sphere-cone aeroshell

Hypersonic phase	m_{entry}, kg
$\beta = 200$ kg/m^2	26,611
$\beta = 400$ kg/m^2	53,222
$\beta = 600$ kg/m^2	79,833

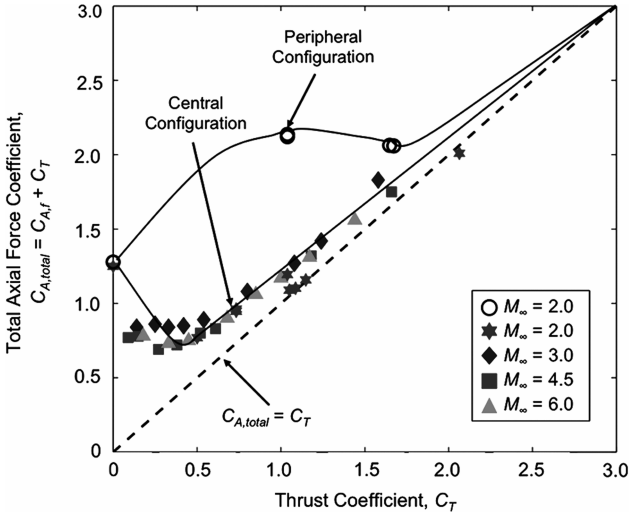

Fig. 3 Experimental data for total axial force coefficient as a function of thrust coefficient [5,7].

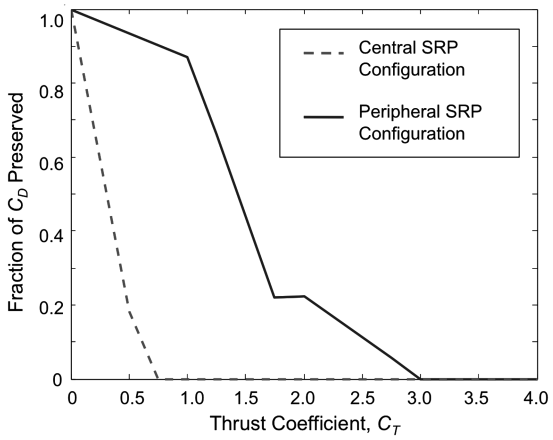

Fig. 4 Aerodynamic–propulsive interactions model (derived from experimental data [5]).

objective. Minimizing the total volume occupied by the propulsion system and also minimizing the total mass of the propulsion system requires a trade-off between mass-efficient performance and available volume within the aeroshell. For example, maximizing the performance of the propulsion system to minimize the total propulsive ΔV requires increasing the available thrust; increasing the available thrust increases the size of the engines but lowers the propellant mass and reduces the size of the propellant tanks. In the supersonic descent phase, the total vehicle mass is updated as a part of the vehicle state at each time step by the relation given in Eq. (3). All T/W values given in this investigation are relative to Martian gravity:

$$\frac{\mathrm{d}m}{\mathrm{d}t} = \frac{-T}{I_{\text{sp}} g_0} \tag{3}$$

The propulsion system is defined to be the propellant, engines, and tanks. The propulsion system is assumed to use LOX/CH_4 ($\rho_{\text{LOX}} = 1140.1$ kg/m^3, $\rho_{CH_4} = 422.6$ kg/m^3) with an I_{sp} of 350 s and mixture ratio of 3.5 [2,15]. This propulsion system choice is consistent with other human-scale Mars EDL studies [2,13–15] and reflects consideration of in situ resource utilization (ISRU) compatibility requirements [9]. Additional discussion on the impact of this assumption is presented in Sec. III.D. The engine mass is scaled with thrust using Eq. (4), a relation developed by Christian et al. [2] through a regression analysis of data for conceptual

LOX/CH_4 engines where T is thrust in N and m_{engine} is the engine mass in kg. Engine volume is conservatively estimated through regression analysis in which a cylindrical volume of equivalent height and diameter for 14 different liquid-bipropellant systems [16] is analyzed against the maximum thrust (in kN) of the engine. The engines, physical dimensions, and thrust characteristics are provided in Table 2, with the resulting regression illustrated in Fig. 5 and given by Eq. (5). Sea-level thrust is given for first stage engines, and vacuum thrust is given for upper stage engines and engines used over a full trajectory to compensate for variations in expansion ratio across the range of propulsion systems used to develop a relationship for engine volume as a function of maximum thrust:

$$m_{\text{engine}} = 0.00144T + 49.6 \tag{4}$$

$$V_{\text{engine}} = 0.0058T + 15.755 \tag{5}$$

The propellant tanks are assumed to be spherical and made of titanium, with an operating pressure of ~1.4 MPa (burst pressure ~2.8 MPa) [2,15]. The tank mass is given by Eq. (6), where m_{tank} is the tank mass in kg, p is the operating pressure in Pa, V is the volume of the propellant in m^3, and ϕ is the tank mass factor (assumed to be 5000 m for titanium) [2,15]:

$$m_{\text{tank}} = \frac{pV}{9.81\phi} \tag{6}$$

All of the cases in this investigation use a 70-deg sphere-cone aeroshell, scaled to 10 m in diameter (shown in Fig. 2). While increasing thrust available increases the mass delivered to the surface by reducing the propellant mass required, the corresponding increase in volume required for the engine results in a net increase in the total volume required for the propulsion system. This net increase in volume required for the propulsion system reduces the volume available for other systems and increases the overall aeroshell packaging density. For consistency with the Apollo and Soyuz capsules [2,15], a 65% usable pressurized volume is assumed in this investigation. Considering that a number of other systems share the remaining unpressurized volume (e.g. thermal protection system, aeroshell support structure), it is desirable that the propulsion system does not exceed 15% of the total aeroshell volume. Beyond 15%, the packaging densities resulting from packaging the remaining mass in the remaining volume approach or exceed those achieved in existing and heritage entry systems.

Figure 6 shows plots of the two objectives for each ballistic coefficient case, with the Pareto-optimal points indicated and increased resolution in the regions of interest.

The Technique for Order Preference by Similarity to Ideal Solution (TOPSIS [17]) is used to select the maximum allowable vehicle T/W based on an ideal solution that minimizes both total propulsion system mass and total propulsion system volume. As seen in Fig. 6, there is no clear choice of $(T/W)_{\max}$ that satisfies both objectives. The Euclidean distance of each alternative (the maximum allowable vehicle T/W) to the ideal solution (the minimum mass and volume for each ballistic coefficient across all $(T/W)_{\max}$ considered) and the relative closeness of each alternative to the ideal solution is used to develop a preferred order of the alternatives. Total propulsion system mass and total propulsion system volume are assumed to have equal weight (50–50) in this analysis.

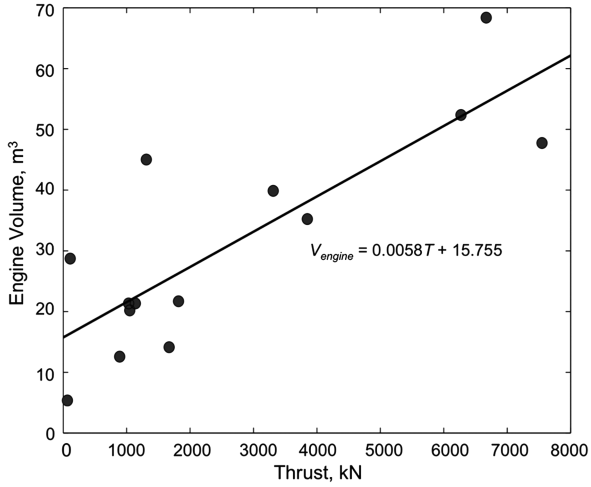

Fig. 5 Regression of engine volume against engine thrust.

The assumption of equally-weighted objectives may not be accurate for a full-scale flight vehicle; the constraint on allowable volume is likely to be more stringent than the constraint on allowable mass. Table 3 summarizes the outcome of the TOPSIS analysis for each ballistic coefficient and illustrates the impact of weighting minimum total propulsion system volume more heavily than total propulsion system mass (60 − 40). As seen in Fig. 6, more $(T/W)_{\max}$ values are considered in the region of the Pareto front to increase resolution; not every $(T/W)_{\max}$ listed in Table 3 is considered for each ballistic coefficient. The columns of Table 3 provide the relative closeness of each alternative to the ideal solution, scaled between 0 and 1. The preferred alternative is the one that is closest to 1, indicated in bold in Table 3. The preferred $(T/W)_{\max}$ for the equal weighting case is used for all subsequent analysis. Note that this value of $(T/W)_{\max}$ is in the range of 3.0 to 4.5.

Table 4 summarizes the outcome of the selection of the maximum allowable vehicle T/W. The final selected maximum allowable vehicle T/W are 3.0, 3.5, and 4.5 for $\beta = 200$, 400, and 600 kg/m^2, respectively. These T/W correspond to the shaded points in Fig. 6. The maximum thrust magnitude for each β is roughly equivalent to four and one-half RL-10 engines, one-half J-2X engine, and one J2-X engine, respectively. The propellant mass fraction (PMF), defined in Eq. (7), for a constant-thrust gravity turn from Mach 0.9, 3 km conditions is included in the propellant masses in Table 4. Bounded by extremes in relative flight path angle at the start of the gravity turn,

Table 2 Summary of liquid-bipropellant engines used in engine volume regression analysis

Engine	Oxidizer/fuel	Thrust, kN	Height, m	Diameter, m	Volume, m^3
RL-10	LOX/LH_2	67	1.73	0.99	5.381
RL-10B2	LOX/LH_2	110	4.14	2.21	28.74
H-1	LOX/RP-1	890	2.68	1.49	12.59
J-2	LOX/LH_2	1033	3.38	2.01	21.34
RS-27A	LOX/RP-1	1050	3.78	1.70	20.19
J-2S	LOX/LH_2	1139	3.38	2.01	21.34
J-2X	LOX/LH_2	1310	4.70	3.05	45.03
RD-253	N_2O_4/UDMH	1670	3.00	1.50	14.14
SSME	LOX/LH_2	1817	4.24	1.63	21.71
RS-68	LOX/LH_2	3312	5.21	2.44	39.89
RD-180	LOX/RP-1	3840	3.56	3.15	35.23
RD-270	N_2O_4/UDMH	6270	4.90	3.40	52.34
F-1	LOX/RP-1	6670	5.79	3.76	68.39
RD-170	LOX/RP-1	7550	3.78	4.02	47.74

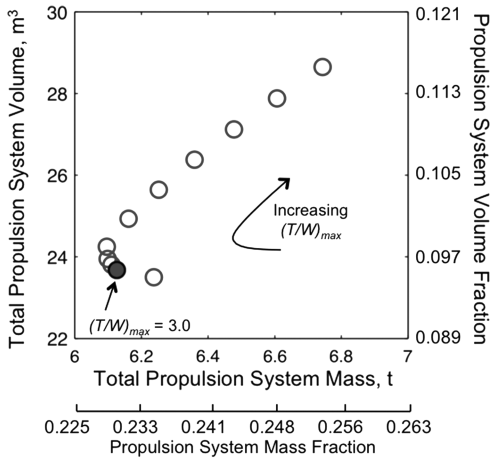

a) $\beta = 200$ kg/m²

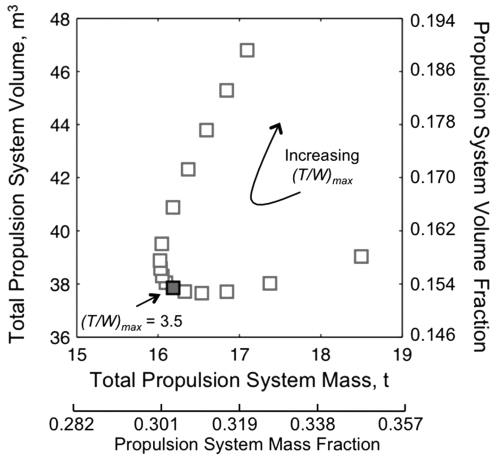

b) $\beta = 400$ kg/m²

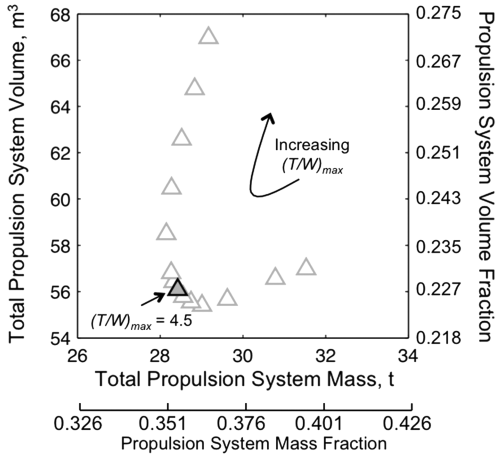

c) $\beta = 600$ kg/m²

Fig. 6 Pareto-optimal design points for a) $\beta = 200$, b) 400, and c) 600 kg/m² (indicated by arrow).

the PMF required for the gravity turn is between 0.137 and 0.169. The $(T/W)_{\max}$ each Pareto-optimal point in Fig. 6 corresponds to does not change as the gravity turn PMF is varied within this given range; however, the total propulsion system mass and volumes do change by the linear relationships given above. The minimum gravity turn PMF (0.137) has been used for the results shown in Fig. 6. No margin has been applied to either wet or dry masses in this investigation. Similar to the effect of varying the subsonic, terminal descent PMF, the application of margin to all sizing results does not affect the Pareto-optimal $(T/W)_{\max}$:

$$\mathrm{PMF} = \frac{m_{\mathrm{prop}}}{m_{\mathrm{entry}}} \tag{7}$$

Supersonic descent PMF is defined to be the ratio of the required propellant mass to reach Mach 0.9 conditions at 3 km altitude to the vehicle mass at SRP initiation. It is significant to notice the difference in Table 4 between the Pareto-optimal results and the minimum supersonic descent PMF results ($\mathrm{PMF}_{\min}$). For each ballistic coefficient considered, the vehicle $(T/W)_{\max}$ that yields the lowest SRP PMF is the upper limit of the T/W range considered ($T/W = 10.0$). However, the $\mathrm{PMF}_{\min}$ results occupy a larger fraction of the aeroshell volume and require a larger total propulsion system mass than the Pareto-optimal results. The consideration of volume and total system mass as two objectives results in a more realistic vehicle $(T/W)_{\max}$ than if total system mass alone had been considered. Note that the goal of total propulsion system volume below 15% of the aeroshell volume (247.2 m³) is achievable only for the $\beta = 200$ and 400 kg/m² cases.

III. Systems Study Results

This section presents the results of a systems-level performance assessment of SRP. Defined are: relevant SRP initiation and operating conditions, propulsion system and overall system performance requirements, and the performance impact of drag preservation during nominal operation (e.g. excluding start up, shut down, engine out, or throttled conditions). The assumptions used in prior studies are assessed, and a brief study of the sensitivity of supersonic PMF to I_{sp} is presented. Lastly, the effect of scale on these trends is illustrated through a sample robotic-scale case. All cases require the ability to fly a lifting hypersonic portion of the trajectory and unless noted otherwise, terminate at Mach 0.9 and 3 km altitude.

A. Bounding Conditions for Initiation and Nominal Operation

Determination of bounding conditions for initiation and nominal operation is approached in two ways: targeting specific conditions and by optimizing the condition to maximize final mass. The most mass-efficient trajectories utilizing SRP will minimize the ΔV provided by the propulsion system (ΔV_{req}), an expression for which is given by Eq. (8). Off-axis thrust losses ($\Delta V_{\mathrm{thrust}}$) are assumed to be negligible in this investigation:

$$\begin{aligned}\Delta V_{\mathrm{req}} &= \Delta V_{\mathrm{ideal}} + \Delta V_{\mathrm{gravity}} - \Delta V_{\mathrm{drag}} + \Delta V_{\mathrm{thrust}} \\ &= I_{\mathrm{sp}} g_0 \ell_n \frac{m_{\mathrm{entry}}}{(m_{\mathrm{entry}} - m_{\mathrm{prop}})} + \int g \sin\gamma \, \mathrm{d}t - \int \frac{D}{m} \, \mathrm{d}t + (\sim 0)\end{aligned} \tag{8}$$

For EDL application and the assumption of a constant I_{sp}, the mass delivered to the surface is maximized for integrated trajectories that minimize gravity losses ($\Delta V_{\mathrm{gravity}}$) and a maximize drag losses (ΔV_{drag}). Provided there is sufficient thrust available and the drag force is not significant, the retropropulsion phase will begin as late as possible (i.e., at the lowest altitude and lowest velocities permitted by the system T/W and other mission constraints), where the thrusting time is the least, to minimize the propellant mass required [from Eq. (3)]. Considering no additional constraints, these mass-optimal SRP trajectories will be characterized by relatively shallow flight path angles at initiation, extended phases of constant-altitude deceleration deep within the atmosphere, and thrust profiles of minimal duration.

Because the SRP aerodynamic–propulsive interaction provides the greatest degree of drag preservation at low thrust coefficients (see Fig. 4), it is possible that the optimal propulsive phase may initiate earlier and decelerate at a reduced thrust level in circumstances where the drag deceleration is significant. Understanding this trade between thrust required, velocity losses, and available timeline is required to bound conditions for initiation and nominal operation for SRP.

To parametrically assess the effect of drag preservation on SRP PMF, initiation velocity and thrust coefficient are decoupled, and specific SRP initiation conditions are targeted. These initial cases

Table 3 TOPSIS results for selection of $(T/W)_{max}$

$(T/W)_{max}$	Equal weighting, $\beta = 200$ kg/m^2	Volume favored, $\beta = 200$ kg/m^2	Equal weighting, $\beta = 400$ kg/m^2	Volume favored, $\beta = 400$ kg/m^2	Equal weighting, $\beta = 600$ kg/m^2	Volume favored, $\beta = 600$ kg/m^2
2.25	——	——	0.559	0.648	——	——
2.50	0.900	0.929	0.737	0.802	——	——
2.75	——	——	0.833	0.877	——	——
3.00	0.958	0.962	0.893	0.921	0.588	0.675
3.25	0.944	0.942	0.934	0.952	0.659	0.737
3.50	0.923	0.918	0.961	0.968	0.800	0.853
3.75	0.901	0.894	0.960	0.959	0.879	0.912
4.00	0.873	0.864	0.941	0.935	0.913	0.937
4.25	——	——	0.917	0.908	0.934	0.947
4.50	——	——	0.891	0.879	0.935	0.938
4.75	——	——	——	——	0.920	0.916
5.00	0.750	0.736	0.835	0.817	0.895	0.887
6.00	0.616	0.600	0.715	0.684	0.779	0.757
7.00	0.472	0.457	0.591	0.546	0.646	0.608
8.00	0.321	0.309	0.467	0.409	0.510	0.454
9.00	0.163	0.156	0.352	0.284	0.383	0.312
10.0	0.000	0.000	0.263	0.196	0.288	0.214

Table 4 Mass and volume summary for Pareto-optimal $(T/W)_{max}$

	Pareto-optimal, $\beta = 200$ kg/m^2	PMF$_{min}$, $\beta = 200$ kg/m^2	Pareto-optimal, $\beta = 400$ kg/m^2	PMF$_{min}$, $\beta = 400$ kg/m^2	Pareto-optimal, $\beta = 600$ kg/m^2	PMF$_{min}$, $\beta = 600$ kg/m^2
Propulsion system mass, kg	5659	6276	15,249	16,159	27,018	27,764
Propellant, kg	5008	4638	13,726	12,811	24,205	22,648
LOX, kg	3895	3607	10,676	9964	18,826	17,615
CH_4, kg	1113	1031	3050	2847	5379	5033
Engines, kg	478.2	1478	1050	2907	1978	4335
Tanks, kg	172.7	159.9	473.3	441.7	834.6	780.9
Propulsion system volume, m^3	23.53	27.11	36.76	42.74	52.76	60.38
Engines, m^3	17.48	21.51	20.17	27.26	23.52	33.02
Propellant, m^3	6.050	5.603	16.58	15.48	29.24	27.36
LOX, m^3	3.417	3.164	9.364	8.739	16.51	15.45
CH_4, m^3	2.633	2.439	7.218	6.736	12.73	11.91
Fraction of aeroshell volume	0.095	0.110	0.149	0.173	0.213	0.244
SRP PMF	0.0682	0.0543	0.1379	0.1207	0.1832	0.1637
T_{max} (kN)	297.6	992.1	694.4	1984	1339	2976
$(T/W)_{max}$ (Mars)	3.0	10.0	3.5	10.0	4.5	10.0

provide valid starting solutions for the full mass-optimal trajectory cases. From experimental data, operating conditions for which there is some degree of drag preservation can be used to define a drag-affected region as a function of the hypersonic vehicle ballistic coefficient in altitude-velocity space. Using Eq. (1) and (2), the dependency of dynamic pressure on vehicle parameters and thrust coefficient can be determined. This relationship is given in Eq. (9), where C_D is the vehicle hypersonic drag coefficient, g_{Mars} is the gravitational acceleration at the surface of Mars, and T/W is the Pareto-optimal $(T/W)_{max}$ determined in Sec. II.D:

$$q_\infty = \frac{T}{C_T A} = \frac{(T/W)_{max} m g_{Mars}}{C_T A} = \frac{(T/W)_{max} \beta C_D g_{Mars}}{C_T} \quad (9)$$

From the relationship given in Eq. (9), a range of initiation conditions to target for the SRP phase can be determined in altitude-velocity space. This range of conditions is not the relevant operational envelope for SRP; however, it is useful in understanding the role of drag preservation in overall EDL system performance by defining initiation conditions to target for parametric analysis. These conditions are constrained by the altitude at which the vehicle reaches Mach 0.9 (with subsequent timeline constraints), Mach number, and dynamic pressure. The dynamic pressure bounds are determined from conditions of nearly full aerodynamic drag preservation ($C_T = 1.0$) and no aerodynamic drag preservation ($C_T = 3.0$). Table 5 gives the dynamic pressure bounds for these two thrust coefficients and $\beta = 200$, 400, and 600 kg/m^2. The upper Mach number bound is determined to be the minimum whole Mach number (five or greater) for which four distinct corner points can be found along the dynamic pressure bounds. Figure 7 illustrates these bounds in altitude—velocity space.

1. Targeted Initiation Condition Results

The four corner points of each shaded region can be used to confirm that lower initiation velocities are preferable, and that for the same initiation velocity, a lower thrust coefficient yields a lower PMF. The hypersonic lifting trajectories are optimized to determine the bank angle profile and atmospheric entry flight path angle yielding a near-zero flight path angle at the target altitude and velocity conditions (corner points defined in Fig. 7) to minimize gravity losses in the subsequent SRP phase. For these targeted cases, the SRP thrust profile and maximum vehicle T/W are determined to

Table 5 Dynamic pressure bounds of a drag-affected region

	$C_T = 1.0$	$C_T = 3.0$
$\beta = 200$ kg/m^2	3.79 kPa	1.26 kPa
$\beta = 400$ kg/m^2	8.82 kPa	2.94 kPa
$\beta = 600$ kg/m^2	17.0 kPa	5.67 kPa

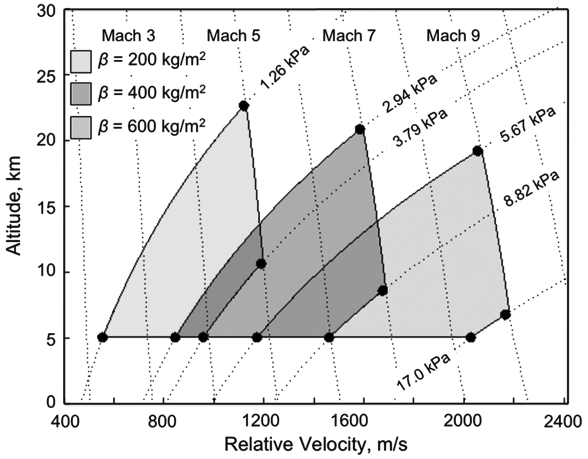

Fig. 7 Trajectory bounds for aerodynamic drag preservation during the retropropulsion phase.

minimize the PMF required to reach the target terminal conditions of Mach 0.9 at 3 km altitude. The resulting trajectories for ballistic coefficients of 200, 400, and 600 $\mathrm{kg/m^2}$ are shown in Figs. 8–10, with a summary of the initiation conditions and required PMF given in Table 6 below. While the SRP initiation boxes are bounded by Mach number, dynamic pressure, and altitude, a small offset of Corner B from the Mach number boundary has been made to allow for an assessment of initiation velocity, and not initiation Mach number, effects.

Between Corners B and C, which have the same initiation velocity, Corner B has a consistently higher PMF required to reach the target. Corner B corresponds to the $C_T = 3.0$ boundary, and Corner C corresponds to the $C_T = 1.0$ boundary. As expected, for the same required velocity change, lower thrust coefficients enable more aerodynamic drag preservation and yield a lower PMF. While there is also a potential energy effect, since Corner B is always significantly higher in altitude than Corner C, this effect is small in comparison to the difference between C_D preservation for $C_T = 1.0$ (Corner C) and $C_T = 3.0$ (Corner B).

Considering pairings of Corners A and B and Corners C and D, which each have the same C_T constraining their initiation conditions, the corners with the lower initiation velocities have a lower PMF. This result is expected, as the PMF should be lower if the ΔV_{drag} contribution to the total ΔV is greater (i.e. the velocity at initiation is lower). The large difference between Corner A and the other three corners for the $\beta = 200$ $\mathrm{kg/m^2}$ case, as compared with the higher ballistic coefficient cases, is primarily due to the thrust requirements under the constraints of constant thrust and fixed initiation conditions exceeding a C_T of 3.0.

Balancing the above two corner comparisons, the impact of initiation velocity is more significant than thrust coefficient at initiation, evidenced by the greater difference in PMF with variation in initiation velocity than with variation in C_T at initiation. In all ballistic coefficient cases examined, Corner A has the lowest PMF, indicating that the optimal initiation conditions are likely to be weighted heavily towards this minimum velocity point (which will occur on the minimum altitude boundary defined by the timeline considerations of the subsequent EDL events.

2. *Mass-Optimal Results*

From the previous results, the lower left corner point (Corner A) is used to target a minimum velocity condition at 5 km altitude. Mass-optimal trajectories are shown as dashed lines in Figs. 8–10, and the

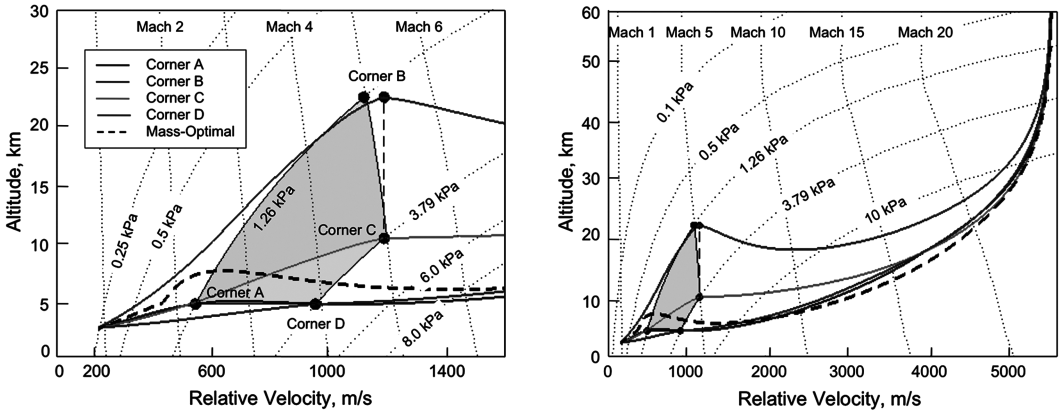

Fig. 8 $\beta = 200$ $\mathrm{kg/m^2}$.

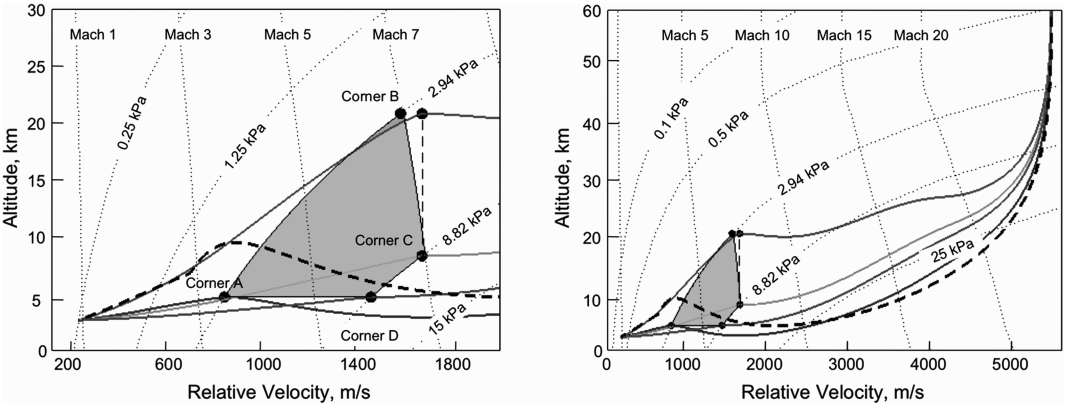

Fig. 9 $\beta = 400$ $\mathrm{kg/m^2}$.

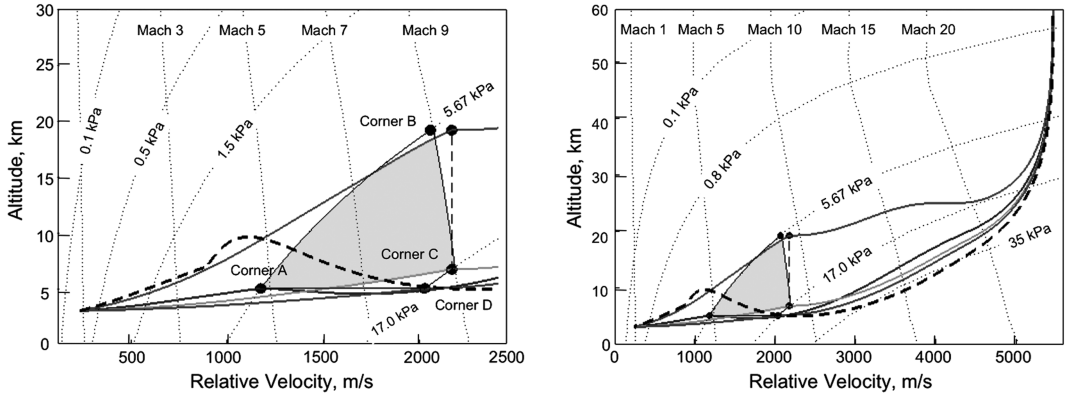

Fig. 10 $\beta = 600$ kg/m^2.

results are given in Table 6 as Pareto-optimal, based on the use of the $(T/W)_{\max}$ determined in Sec. II.D. Note that the mass-optimal cases for $\beta = 400$ and 600 kg/m^2 require a minimum altitude constraint of 5 km during the hypersonic phase to prevent solutions with unrealistic minimum altitudes prior to SRP initiation.

Figures 8–11 illustrate the characteristics of the hypersonic phase of Mars entry trajectories for vehicles utilizing SRP across ballistic coefficients from 200 to 600 kg/m^2. For all three ballistic coefficients considered, the vehicle initially dives deeply into the atmosphere and then banks to fly an extended, near-constant-altitude deceleration profile until SRP initiation at low-to-mid supersonic conditions. All three cases show a 3-to-5 km loft at supersonic conditions, prior to SRP initiation. The 5 km minimum altitude limit affects the $\beta = 400$ and 600 kg/m^2 cases; the vehicle flies along this minimum altitude boundary before lofting.

Peak deceleration (given in Earth g's) occurs during the hypersonic phase (Fig. 11). As ballistic coefficient increases, the relative entry flight path angle shallows, resulting in the reduction in peak deceleration magnitude shown in Fig. 11. While these sustained decelerations may exceed limits for human crew [2,10], they are likely acceptable for high-mass cargo missions.

The scale of the vehicles considered here likely results in significant turbulent heating away from the stagnation-point. Increased turbulent heating shifts the peak heating location towards the leeward shoulder and significantly increases both heat flux and shear [18]. The model developed by Steinfeldt et al. [15] for peak heat rate (laminar and turbulent) is used here and given in Eq. (10):

$$\dot{q} = (2.65 \times 10^{-12})\rho_{\infty}^{0.913} v_{\infty}^{4.51} \left(\frac{1.125}{r_n}\right)^{1/2} \tag{10}$$

This model is based on work by Tauber [19] for heating at the stagnation-point and Eckert's method [20] for acreage heating. Using this model to approximate the peak convective heat rate (laminar and turbulent) for $\beta = 200$, 400, and 600 kg/m^2, the peak convective heat rates are 192.3, 295.7, and 294.2 W/cm^2, respectively. These heat rates are between 4.3 and 5.2 times greater than the peak heat rates calculated using Chapman's equation [21], which approximates laminar convective heating at the stagnation point. The similarity between the $\beta = 400$ kg/m^2 and $\beta = 600$ kg/m^2 cases is due to both cases being actively constrained by the 5 km minimum altitude bound. While these peak heat rates are high as a result of assuming a direct entry, they are still well within the capabilities of existing TPS materials (e.g. PICA) [22].

Table 6 and Fig. 11 summarize the SRP initiation conditions for the three Pareto-optimal cases. Initiation occurs between Mach 1.80 and Mach 3.64 at altitudes ranging from 5.12 km to 7.05 km. In all cases, initiation occurs on the downside of a 3-to-5 km loft. This loft allows the vehicle to gain timeline and helps reduce the propulsive ΔV by delivering the vehicle to initiation conditions that minimize the amount of time required as a function of the thrust available. The thrust history (Fig. 11) shows little or no throttling required, though a throttle range from 0 to 100% was permitted during optimization.

Figure 11 gives the SRP thrust, thrust coefficient, and dynamic pressure histories. C_T at initiation, by Eq. (2), is the minimum C_T for

Table 6 SRP phase initiation conditions and PMF results

	Altitude, km	Relative velocity, m/s	Mach number	Relative flight path angle, deg	Max vehicle T/W	Max thrust, kN	PMF	Total propulsive ΔV, m/s
				$\beta = 200$ kg/m^2				
Pareto-optimal	5.124	441.35	1.80	**−13.45**	3.00	297.6	0.0683	242.9
Corner A	5.000	549.8	2.24	0.0	3.27	324.4	0.0962	347.3
Corner B	22.54	1183	5.21	0.0	2.59	256.6	0.2699	1080
Corner C	10.58	1183	4.91	0.0	4.16	413.1	0.2538	1005
Corner D	5.000	952.2	3.87	0.0	6.87	681.7	0.1945	742.6
				$\beta = 400$ kg/m^2				
Pareto-optimal	7.049	697.5	2.86	**−8.44**	3.5	694.4	0.1379	509.5
Corner A	5.000	839.8	3.42	0.0	5.76	1143	0.1681	631.9
Corner B	20.75	1668	7.27	0.0	3.59	711.7	0.3589	1526
Corner C	8.537	1668	6.87	0.0	7.01	1390	0.3481	1469
Corner D	5.000	1455	5.92	0.0	11.18	2117	0.3033	1241
				$\beta = 600$ kg/m^2				
Pareto-optimal	6.966	889.1	3.64	**−6.396**	4.5	1339	0.1832	694.8
Corner A	5.000	1166	4.75	0.0	8.45	2515	0.2427	954.5
Corner B	19.11	2158	9.32	0.0	4.63	1377	0.4403	1993
Corner C	6.711	2158	8.83	0.0	10.93	3252	0.4329	1948
Corner D	5.000	2020	8.22	0.0	15.23	4533	0.4087	1804

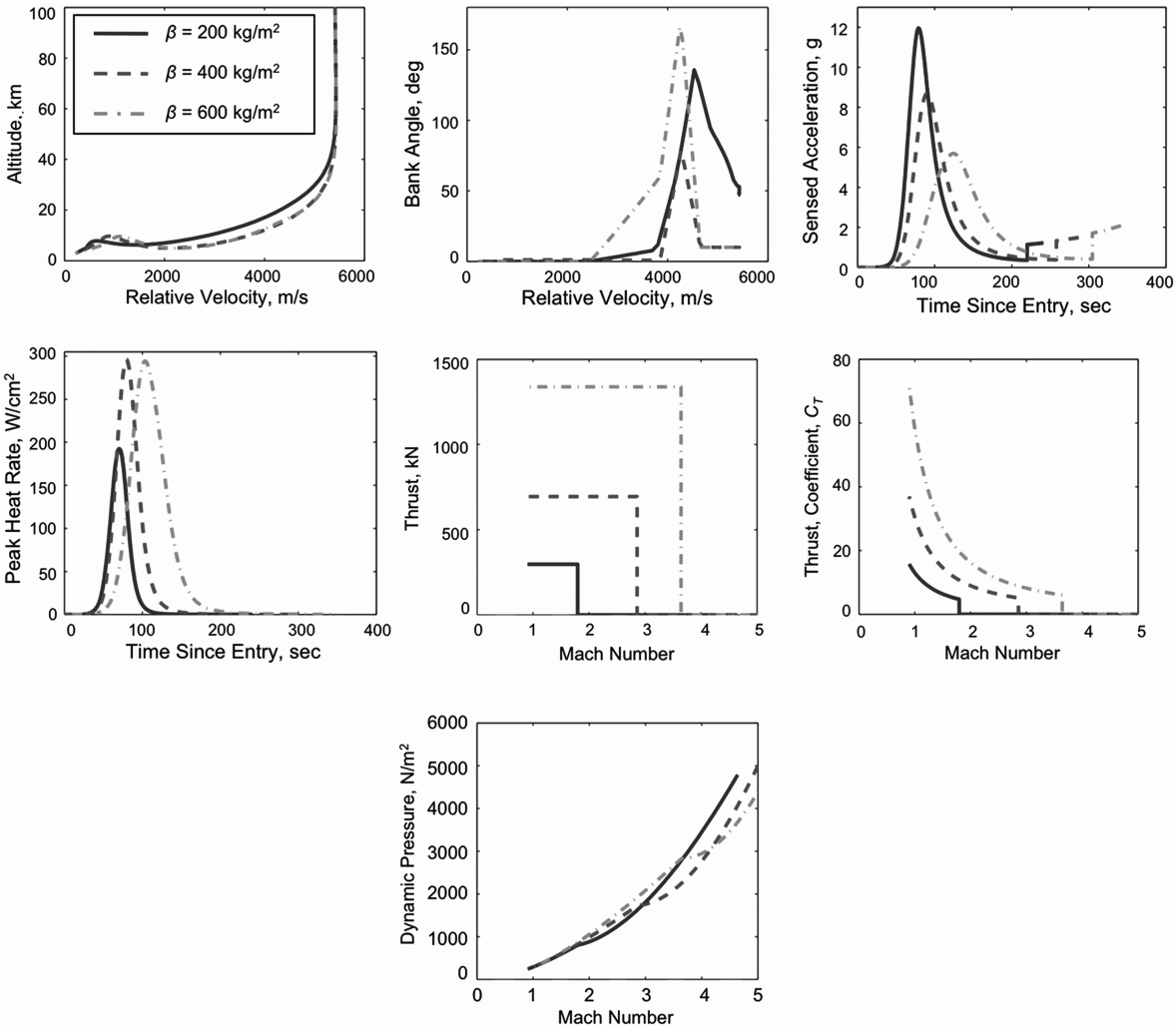

Fig. 11 Comparison of hypersonic and SRP trajectory histories with vehicle ballistic coefficient.

the entire retropropulsion phase. For $\beta = 200$, 400, and 600 kg/m^2, the minimum C_T's are 4.72, 5.11, and 6.03, respectively. Experimental data shows no C_D preservation above $C_T \sim 3$ [4–9], confirming the agreement of SRP initiation trends with analytic models that consider thrust as the only contributor to axial force, despite the inclusion of a condition-dependent drag preservation model in this investigation. The significance of drag preservation during SRP is discussed further in Sec. III.B.

Comparing the Pareto-optimal trajectories to the targeted corner point trajectories in Sec. III.A.1, the Pareto-optimal trajectories all require less propulsive ΔV, comparatively lower thrust magnitudes, lower initiation Mach numbers, higher thrust coefficients, and steeper initiation flight path angles. The significant difference between the most mass-efficient targeted corner point trajectories and the Pareto-optimal trajectories is the supersonic loft prior to initiation, delivering the vehicle to the conditions most suitable for minimizing the propellant mass required as a function of the thrust available.

B. Significance of Drag Preservation During SRP

As shown in the previous section, maximum drag preservation during SRP ($C_T \leq 1$) results in thrust conditions that are suboptimal with respect to the PMF required to achieve Mach 0.9 conditions at 3 km altitude. A $\beta = 400$ kg/m^2 sample case was considered with varying degrees of drag preservation during SRP to address the question: how much drag preservation is needed to have a significant performance impact? In this portion of the analysis, 0% to 200% of the supersonic static aerodynamic drag coefficient is preserved during SRP, independent of thrust coefficient, to highlight the effect of drag preservation on the trends discussed in Sec. III.A. Note that it is unknown if realistic retropropulsion configurations can be developed that provide the extreme degrees of aerodynamic drag augmentation considered here. The supersonic drag coefficient representing 100% is assumed to be 1.58.

Figure 12 shows the reduction in PMF as the degree of drag preservation is increased for three constraints on the minimum allowable thrust magnitude: $T_{\min} = T_{\max}$, $T_{\min} = 0.5T_{\max}$, $T_{\min} = 0.1T_{\max}$. Constraints on the minimum allowable thrust magnitude are required to prevent solutions with no thrust and more than 100% of the supersonic C_D preserved. Preservation of drag during the SRP phase results in a departure from the "maximum available thrust for the minimum time" trend described in Sec. III.A. The objective to minimize ΔV_{prop} requires maximizing ΔV_{drag}. Recalling Eq. (7), this translates to minimizing thrusting time and maximizing time for aerodynamic drag.

Up to 100% C_D preserved, the addition of drag to thrust results in a delayed initiation and a reduction in PMF, as drag is a small, but penalty-free, contribution to the total axial force decelerating the vehicle. Beyond 100% C_D preservation, beginning the SRP phase earlier becomes beneficial; C_D with thrust is greater than C_D with no thrust. As the drag available becomes significant as compared with the thrust available, there is a balance between maximizing time for drag and minimizing time for thrust to minimize the required propulsive ΔV. This departure becomes significant at $\sim C_D = 1.9$, as shown in Fig. 12. More generally, SRP initiation trends begin to change when the ratio of C_D to $C_{A,\text{total}}$ ($C_D + C_T$) exceeds ~25%.

Table 7 summarizes the change in propulsive and drag contributions to the total ΔV as the degree of drag preservation is

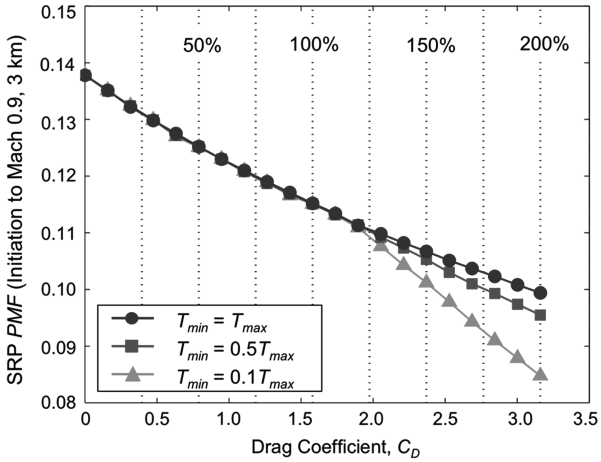

Fig. 12 Impact of drag preservation on supersonic descent PMF.

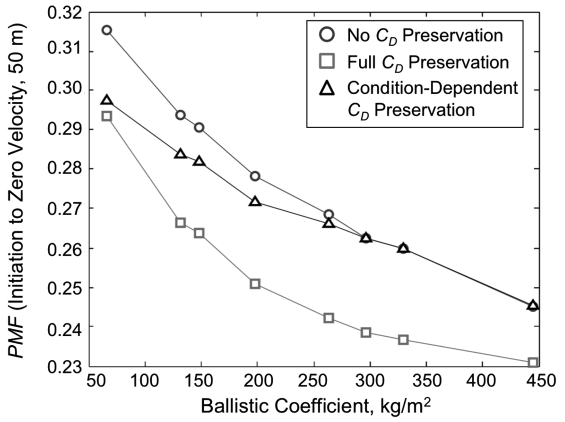

Fig. 13 Comparison of C_D preservation assumptions during SRP.

increased. From Eq. (8), ΔV_{drag} is integrated over the entire SRP phase. For the $T_{\min} = T_{\max}$ case, the thrust profile is constant, resulting in a near-linear decrease in SRP PMF with increasing C_D preservation. The $T_{\min} = 0.5T_{\max}$ and $T_{\min} = 0.1T_{\max}$ cases illustrate the significance of drag preservation at low-to-moderate thrust levels. In these cases, SRP initiates earlier, with initial thrust magnitudes equal to the minimum allowable thrust for increasing duration as the degree of C_D preservation is increased.

Drag preservation during SRP, if possible, can result in significant reductions in propellant required. However, considering the $\beta = 400$ kg/m^2 sample case, 100% drag preservation only reduces the required propellant mass by ~1200 kg (or 2.26%) as compared with no drag preservation. Alternatively, the ability to preserve a portion of the aerodynamic drag during SRP may be more significant in reducing the volume required for the propulsion system by allowing the use of smaller engines and less propellant for the same total deceleration. Though not considered here, the greatest potential benefit of drag preservation during SRP may be in extending or enhancing control authority through supersonic descent. Uncertainties in the stability of the aerodynamic–propulsive interaction at lower thrust coefficients are an unfavorable consequence of SRP [4], and significant benefit in packaging, performance, and control authority would likely need to be realized for an aerodynamic drag contribution to retropropulsion to be considered by mission designers.

Table 7 Effect of drag preservation during SRP

% C_D preserved	M_{init}	ΔV_{drag}, m/s	ΔV_{prop}, m/s	Time, s	SRP PMF
		$T_{\min} = T_{\max}$			
0	2.86	0	509.2	36.26	0.1378
50	2.81	39.03	459.3	32.94	0.1252
100	2.78	68.82	420.2	30.30	0.1152
120	2.76	79.31	405.0	29.27	0.1113
140	2.75	93.55	393.3	28.47	0.1082
160	2.74	102.0	381.2	27.64	0.1051
180	2.73	108.2	370.6	26.91	0.1023
200	2.72	118.5	359.5	26.15	0.0994
		$T_{\min} = 0.5T_{\max}$			
0	2.86	0	508.8	36.23	0.1380
50	2.81	38.49	459.3	32.94	0.1252
100	2.79	71.34	419.8	31.08	0.1151
120	2.80	92.52	405.4	31.63	0.1114
140	2.83	114.4	389.6	33.46	0.1073
160	2.86	144.6	373.3	36.05	0.1030
180	2.85	153.4	358.9	34.73	0.0993
200	2.90	185.8	344.6	37.42	0.0955
		$T_{\min} = 0.1T_{\max}$			
0	2.86	0	509.2	36.26	0.1378
50	2.81	38.99	459.3	32.90	0.1251
100	2.78	71.53	420.0	30.84	0.1151
120	2.96	136.3	403.8	41.66	0.1109
140	3.10	197.5	378.3	49.47	0.1043
160	3.31	282.3	353.2	60.55	0.0978
180	3.36	322.7	327.6	61.60	0.0910
200	3.46	373.9	304.2	66.94	0.0848

C. Assessment of SRP Modeling Assumptions

A comparison with a prior human-scale Mars EDL study by Christian et al. [2] is completed to illustrate the potential impact of assuming C_D preservation during the SRP phase. The prior study assumed the SRP phase to be modeled by a constant-thrust gravity turn control law with the aerodynamic drag fully preserved and zero lift. The vehicle followed a constant-thrust trajectory to a zero-velocity terminal condition 50 m above the surface. The gravity turn control law requires the thrust vector to be maintained in the direction opposite the vehicle's relative velocity vector and the thrust magnitude to be constant. The SRP initiation time was varied to minimize the sum of the propellant and propulsion system masses.

For consistency with the prior study, the vehicle configuration is assumed to be a 15 m-diam Apollo aeroshell with a LOX/CH_4 propulsion system. All trajectories start from orbit (4 km/s) with an inertial entry flight path angle of $-14.5°$. The trajectories are constrained to a 5-g-Earth limit. The design points for this comparison are for pure lift-up and lift-down trajectories. For consistency, the design points from this study assume a constant-thrust magnitude, constrained to be no larger than 1 MN. The thrust magnitude and initiation conditions are varied to minimize the total propulsion system mass; however, a condition-dependent model for C_D preservation is active during the SRP phase. The aerodynamic–propulsive interactions model for these cases applies the fraction of C_D preserved to the no-thrust C_D of an Apollo aeroshell instead of a 70-deg sphere-cone. For comparison against these two SRP modeling approaches, the same cases were simulated assuming no C_D preservation during the gravity turn.

Figure 13 shows the difference between the three C_D preservation assumptions as vehicle ballistic coefficient increases for the $L/D = 0.3$ cases. The complete results are summarized in Table 8. The data in Table 8 include results from both 10 and 15 m-diam aeroshells. Table rows with no data are cases that were not able to satisfy the desired terminal conditions without violating the maximum allowable thrust or 5-g deceleration constraints.

Figure 13 illustrates that the condition-dependent drag preservation model is better aligned with the assumption of full drag preservation at low vehicle ballistic coefficients and better aligned with the assumption of no drag preservation for ballistic coefficients above approximately 300 kg/m^2. Since most human-scale Mars exploration architectures that utilize blunt bodies are characterized by large ballistic coefficient vehicles [2,14,15], these system studies would be more accurately performed by assuming no aerodynamic drag preservation (or the aerodynamic–propulsive interactions

Table 8 Results from comparison of SRP modeling assumptions

	Initial Mass, kg	No C_D preservation, PMF	Thrust, kN	Condition-dependent C_D preservation, PMF	Thrust, kN	Full C_D preservation, PMF	Thrust, kN	% difference (between cond. and no C_D)	% difference (between cond. and full C_D)
				$L/D = 0.3$					
$\beta = 65.94$ kg/m^2	18,411	0.315	102.8	0.297	85.57	0.294	70.9	5.90	1.27
$\beta = 131.9$ kg/m^2	36,823	0.294	240.1	0.284	221.1	0.266	176.7	3.49	6.30
$\beta = 148.4$ kg/m^2	18,411	0.291	121.7	0.282	113.0	0.264	91.1	3.07	6.65
$\beta = 197.8$ kg/m^2	55,234	0.278	417.7	0.272	396.9	0.251	319.5	2.43	7.93
$\beta = 263.8$ kg/m^2	73,645	0.268	660.6	0.266	651.5	0.242	523.6	0.83	9.44
$\beta = 296.7$ kg/m^2	36,823	0.262	358.2	0.262	358.2	0.238	290.0	0.00	9.58
$\beta = 329.7$ kg/m^2	92,057	0.260	976.0	0.260	976.0	0.237	805.6	0.00	9.33
$\beta = 445.1$ kg/m^2	55,234	0.245	1027	0.245	1027	0.231	916.3	0.03	6.03
$\beta = 593.5$ kg/m^2	73,645	——	——	——	——	——	——	——	——
$\beta = 741.8$ kg/m^2	92,057	——	——	——	——	——	——	——	——
				$L/D = 0.5$					
$\beta = 65.94$ kg/m^2	18,411	0.308	108.9	0.283	77.3	0.284	72.4	8.55	0.41
$\beta = 131.9$ kg/m^2	36,823	0.285	263.9	0.270	233.0	0.253	186.9	5.33	6.48
$\beta = 148.4$ kg/m^2	18,411	0.281	139.2	——	——	0.248	99.9	——	——
$\beta = 197.8$ kg/m^2	55,234	0.271	477.3	0.263	447.5	0.240	356.8	2.93	8.90
$\beta = 263.8$ kg/m^2	73,645	0.260	813.6	0.259	806.0	0.233	643.3	0.31	10.40
$\beta = 296.7$ kg/m^2	36,823	0.255	454.3	0.256	454.3	0.232	369.4	0.38	9.74
$\beta = 329.7$ kg/m^2	92,057	0.250	1408	0.250	1408	0.229	1185	0.00	8.67
$\beta = 445.1$ kg/m^2	55,234	——	——	——	——	——	——	——	——
$\beta = 593.5$ kg/m^2	73,645	——	——	——	——	——	——	——	——
$\beta = 741.8$ kg/m^2	92,057	——	——	——	——	——	——	——	——

model defined in this investigation) than full drag preservation. In addition, Fig. 13 demonstrates that human-scale Mars exploration missions that utilize slender body aeroshells (generally characterized by lower ballistic coefficients) may be more suited for application of SRP technology. However, to make definitive statements in this regard, a SRP aerodynamic interactions model for a slender body entry configuration must be developed.

D. Sensitivity to I_{sp}

The results presented in Secs. III.A and III.B all assume a constant I_{sp} of 350 s, with the maximum thrust magnitude constrained by the Pareto-optimal $(T/W)_{max}$ at SRP initiation. While varying I_{sp} will change the total propulsion system volume and total propulsion system mass, it is assumed that the sensitivity of the Pareto-optimal $(T/W)_{max}$ to I_{sp} is negligible. In consideration of propellant combinations other than LOX/CH_4, a sweep of I_{sp} for the $\beta =$ 400 kg/m^2 case is completed. As expected, the trend shown in Fig. 14 below is consistent with Eq. (3). Between 250 and 550 s, there is a 70.2% difference in PMF, or ~5045 kg of propellant.

Table 9 compares the impact of I_{sp} on system performance and sizing using sample LOX/RP-1, LOX/CH_4, and LOX/LH_2 propulsion systems. The sample systems all have a maximum thrust magnitude that is comparable to 694.4 kN, T_{max} for the $\beta =$ 400 kg/m^2 case. The propulsive ΔV is assumed to be equal for all three propulsion systems compared. The LOX/CH_4 propulsion system is the same system used in all previous trades in this investigation. The propellant densities for LOX, RP-1, CH_4, and LH_2 are 1140.1 kg/m^3, 820 kg/m^3, 422.6 kg/m^3, and 70 kg/m^3, respectively.

Figure 14 and Table 9 illustrate that increasing I_{sp} reduces the required propellant mass. As discussed earlier, the volume occupied by the propulsion system is likely to be of equal or more importance than the overall system mass. While using significantly less propellant overall, the LOX/LH_2 system requires more than twice the propellant volume of the LOX/RP-1 and LOX/CH_4 systems to provide the same propulsive ΔV. Provided that a LOX/CH_4 propulsion system can be developed that satisfies the thrust, control, and throttling requirements of both SRP and terminal descent, a requirement that the propulsion system be ISRU-compatible [10] is likely not detrimental to the overall EDL system sizing and performance.

E. Application to Future Robotic Mission

A sample future robotic EDL configuration is derived based on MSL, with an entry mass of 5 t, a 4.5-m-diam 70-deg sphere-cone aeroshell, and use of the MSL Mars lander engines (MLEs). A single MLE is assumed to have a maximum thrust of 3000 N and an I_{sp} of 225 s (hydrazine propellant) [23]. A single descent stage with 12 MLEs is used for all deceleration not derived from the vehicle's aerodynamic drag. The MSL descent stage has 8 MLEs; the use of 12 MLEs increases the vehicle $(T/W)_{max}$ from 1.23 to 1.94 (Mars-relative) for a 5 t vehicle.

Two cases are compared: one where no C_D preservation was allowed during SRP and one where a fraction of the no-thrust C_D was preserved as a function of the thrust magnitude and current dynamic pressure [based on Eq. (9)]. A relative entry flight path angle of −13.65° is assumed and a variable bank angle profile utilized in the hypersonic phase of flight. The conditions at SRP initiation and the thrust profile are allowed to vary to minimize the propellant mass required to decelerate to a terminal condition of 2.5 m/s at 50 m above the ground. From these two optimizations, a summary of the differences in required SRP initiation conditions and propellant required is given in Table 10 below.

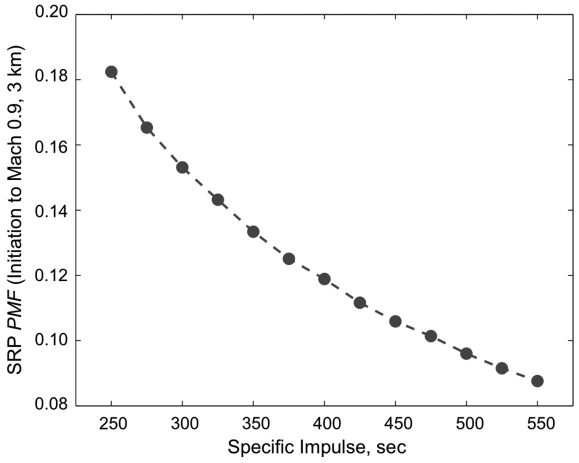

Fig. 14 Variation in SRP PMF with I_{sp}.

Table 9 Effect of I_{sp} (vacuum) on system performance and sizing

I_{sp}, s	289	350	421
Engine	H-1	Theoretical	J2-X
Ox/fuel	LOX/RP-1	LOX/CH_4	LOX/LH_2
Mixture ratio	2.25	3.50	5.50
ΔV, m/s	490.8	490.8	490.8
Prop. mass, kg	8447	7089	5963
Oxidizer mass, kg	5848	5514	5046
Fuel mass, kg	2599	1575	917.4
Prop. vol., m^3	8.30	8.56	17.53
Oxidizer vol., m^3	5.13	4.84	4.43
Fuel vol., m [3]	3.17	3.73	13.12
PMF	0.1587	0.1332	0.1120

Table 10 SRP performance for a 5 t robotic case

	SRP C_D preserved	No C_D preserved	Delayed initiation
		Initiation	
M_∞	2.85	2.96	1.82
C_T	2.20	2.16	5.87
Altitude, km	12.95	13.67	2.76
q_∞, Pa	1032	1046	996.2
		Performance	
$(T/W)_{max}$	1.94	1.94	5.0
m_{prop}, kg	1594	1664	1010
PMF	0.319	0.333	0.202

A third case is considered, with a vehicle $(T/W)_{max}$ of 5.0 for comparison; the results are given in Table 10. Increasing the available thrust (by increasing T/W) allows the vehicle to initiate SRP later in the trajectory, using the vehicle's aerodynamic drag to reduce the total propulsive ΔV. The increase in $(T/W)_{max}$ from 1.94 to 5.0 reduces the required ΔV by 230 m/s, as compared to the original case with condition-dependent C_D preservation, and by 251 m/s as compared to the original case with no C_D preservation.

Considering the two cases with a $(T/W)_{max} = 1.94$, the 70-kg difference in required propellant mass (a PMF difference of 4.5%) and the difference in initiation conditions show the impact of C_D preservation during the descent phase. For these cases, the maximum thrust available from the 12 MLEs is low enough for C_T to be below 3.0 until the vehicle has decelerated to approximately Mach 2.0. For the $(T/W)_{max} = 1.94$ case with no C_D preservation, this translates into SRP initiation earlier in the trajectory (higher altitude and Mach number) than for the case with C_D preservation. This is illustrated in Fig. 15 below. Though the thrust profile was not constrained to be constant, the final profiles were of near-constant thrust in both cases.

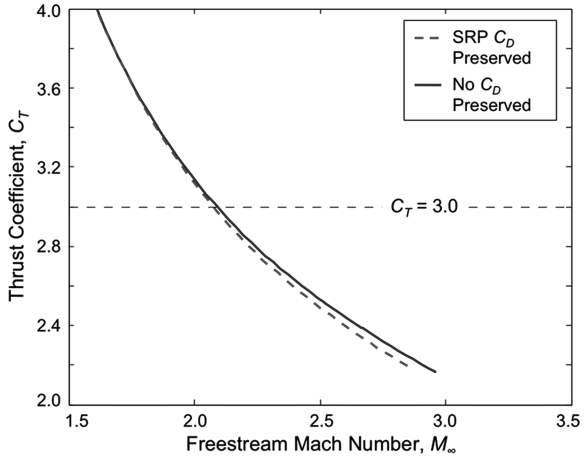

Fig. 15 Thrust coefficient profile for robotic cases ($(T/W)_{max} = 1.94$).

IV. Conclusions

As vehicle mass increases for missions involving atmospheric entry, supersonic deceleration is challenging the qualifications and capabilities of Viking-heritage EDL technology. At Mars, high entry masses and insufficient atmospheric density often result in unacceptable parachute deployment and operating conditions, requiring the exploration of alternative approaches to supersonic deceleration. SRP may be an enabling technology for systems that aim to decelerate large masses in a thin atmosphere, such as at Mars.

Across a wide range of ballistic coefficients, mass-optimal Mars entry trajectories for vehicles utilizing SRP are characterized by extended phases of near-constant-altitude deceleration deep within the atmosphere, shallow flight path angles at SRP initiation to minimize gravity losses, and initiation conditions that minimize the required propulsive ΔV. These conditions generally imply SRP initiation at the minimum altitude boundary defined by the timeline considerations of subsequent EDL events. Overall, a lower initiation velocity is strongly preferable over a lower C_T. The peak deceleration magnitudes in this analysis are likely acceptable for cargo, though not for a deconditioned human crew, and occur during the hypersonic phase of the trajectory. SRP initiation conditions are a strong function of the thrust available, and for all cases considered here, the SRP phase relies on no drag preservation to reach subsonic conditions with timeline margin. The 70-deg sphere-cone aeroshell ($L/D_{max} = 0.24$) is capable of delivering the vehicle to a significant range of SRP initiation conditions.

While minimizing the propulsion system mass increases the mass delivered to the surface, the increased volume required for the propulsion system increases the aeroshell packaging densities significantly. Considering the minimization of total propulsion system volume as an equally important objective to minimizing propulsion system mass results in a lower $(T/W)_{max}$ than if mass is considered alone. If a retropropulsion configuration can be developed that preserves a portion of the aerodynamic drag during SRP without significant flow instabilities, such a configuration may be most advantageous in reducing the volume required for the propulsion system or extending control authority through supersonic descent.

For blunt body entry systems and a constant-thrust profile, assuming no C_D preservation during SRP is conservative for hypersonic $\beta \leq 250$ kg/m^2. For blunt body entry systems with a hypersonic $\beta \geq 300$ kg/m^2, the thrust coefficient required implies that aerodynamic drag cannot be preserved. As such, human-scale Mars exploration blunt body entry systems studies are most accurately performed by assuming no aerodynamic drag preservation (or the aerodynamic–propulsive interactions model defined in this investigation) rather than full drag preservation. In addition, while analysis of a 5 t robotic-scale mission demonstrated a 4.5% PMF advantage to SRP drag preservation, the T/W limitations of the propulsion system assumed in this study constrained SRP initiation to a high altitude, high velocity condition that was shown to be relatively inefficient in comparison to a higher T/W system design.

Past experimental work has demonstrated SRP on a small scale, establishing trends in static aerodynamics as a function of retropropulsion configuration, freestream conditions, and thrust. The results from this investigation are strongly dependent on the assumed peripheral retropropulsion configuration and limited experimental data. Based on work to date, it is expected that these trends will extend to higher ballistic coefficients as additional SRP configurations are studied and the complexity and fidelity of the models are increased.

Acknowledgments

This work was funded through a contract from the NASA Fundamental Aeronautics Program: Hypersonics Project. The authors would like to thank Bradley Steinfeldt of the Georgia Institute of Technology Space Systems Design Laboratory for his assistance with the system sizing and $(T/W)_{max}$ determination in this investigation. The authors would also like to thank Ian Clark of the Jet Propulsion Laboratory and the NASA Exploration Technology

Development Program supersonic retropropulsion team for their review and support of this work.

References

[1] Braun, R. D., and Manning, R. M., "Mars Exploration Entry, Descent, and Landing Challenges," *Journal of Spacecraft and Rockets*, Vol. 44, No. 2, 2007, pp. 310–323. doi:10.2514/1.25116

[2] Christian, J. A., Wells, G. W., Lafleur, J. M., Verges, A. M., and Braun, R. D., "Extension of Traditional Entry, Descent, and Landing Technologies for Human Mars Exploration," *Journal of Spacecraft and Rockets*, Vol. 45, No. 1, 2008, pp. 130–141. doi:10.2514/1.31929

[3] Korzun, A. M., Cordell, C. E., Jr., and Braun, R. D., "Comparison of Inviscid and Viscous Aerodynamic Predictions of Supersonic Retropropulsion Flowfields," AIAA Paper 2010-5048, June 2010.

[4] Korzun, A. M., Braun, R. D., and Cruz, J. R., "Survey of Supersonic Retropropulsion Technology for Mars Entry, Descent, and Landing," *Journal of Spacecraft and Rockets*, Vol. 46, No. 5, 2009, pp. 929–937. doi:10.2514/1.41161

[5] Jarvinen, P. O., and Adams, R. H., "The Aerodynamic Characteristics of Large Angled Cones with Retrorockets," NASA CR NAS 7-576, Feb. 1970.

[6] Romeo, D. J., and Sterrett, J. R., "Exploratory Investigation of the Effect of a Forward-Facing Jet on the Bow Shock of Blunt Body in a Mach Number 6 Free Stream," NASA TN D-1605, Feb. 1963.

[7] McGhee, R. J., "Effects of a Retronozzle Located at the Apex of a 140° Blunt Cone at Mach Numbers of 3.00, 4.50, and 6.00," NASA TN D-6002, Jan. 1971.

[8] Peterson, V. L., and McKenzie, R. L., "Effects of Simulated Retrorockets on the Aerodynamic Characteristics of a Body of Revolution at Mach Numbers from 0.25 to 1.90," NASA TN D-1300, May 1962.

[9] Keyes, J. W., and Hefner, J. N., "Effect of Forward Facing Jets on Aerodynamic Characteristics of Blunt Configurations at Mach 6," *Journal of Spacecraft and Rockets*, Vol. 4, No. 4, 1967, pp. 533–534. doi:10.2514/3.28900

[10] Drake, B. G. (ed.), "Human Exploration of Mars: Design Reference Architecture 5.0," NASA SP-2009-566, July 2009.

[11] Streipe, S. A., Powell, R. W., Desai, P. N., Queen, E. M., Brauer, G. L., Cornick, D. E., Olson, D. W., Petersen, F. M., Stevenson, R., Engel, M. C., Mars, S. M., and Gromko, A. M., "Program to Optimize Simulated Trajectories (POST II): Utilization Manual, Volume 2, Version 1.16.G," NASA Langley Research Center, 2004.

[12] Spencer, D. A., Blanchard, R. C., Braun, R. D., Kallemeyn, P. H., and Thurman, S. W., "Mars Pathfinder Entry, Descent, and Landing Reconstruction," *Journal of Spacecraft and Rockets*, Vol. 36, No. 3, 1999, pp. 357–366. doi:10.2514/2.3478

[13] Marsh, C. L., and Braun, R. D., "Fully-Propulsive Mars Atmospheric Transit Strategies for High-Mass Payload Missions," IEEEAC Paper 1219, March 2009.

[14] Price, H., Hawkins, A. M., and Radcliffe, T. O., "Austere Human Missions to Mars," AIAA Paper 2009-6685, Sept. 2009.

[15] Steinfeldt, B. A., Theisinger, J. E., Korzun, A. M., Clark, I. G., Grant, M. J., and Braun, R. D., "High Mass Mars Entry, Descent, and Landing Architecture Assessment," AIAA Paper 2009-6684, Sept. 2009.

[16] Sutton, G. P., and Biblarz, O., *Rocket Propulsion Elements*, 7th ed., Wiley-Interscience, New York, 2001.

[17] Kirby, M. R., and Mavris, D. N., "A Method for Technology Selection Based on Benefit, Available Schedule and Budget Resources," AIAA Paper 2000-5563, Oct. 2000.

[18] Edquist, K. T., Dyakonov, A. A., Wright, M. J., and Tang, C. Y., "Aerothermodynamic Environments Definition for the Mars Science Laboratory Entry Capsule," AIAA Paper 2007-1206, Jan. 2007.

[19] Tauber, M. E., "A Review of High-Speed Convective, Heat-Transfer Computational Methods," NASA TP 2914, 1989.

[20] Kinney, D. J., "Aero-Thermodynamics for Conceptual Design," AIAA Paper 2004-31, Jan. 2004.

[21] Chapman, D. R., "An Approximate Analytical Method for Studying Entry into Planetary Atmospheres," NASA TR R-11, 1959.

[22] Davies, C. (ed.), "Planetary Mission Entry Vehicle Quick Reference Guide, Version 3.0," NASA SP-2006-3041, 2006.

[23] Way, D. W., Powell, R. W., Chen, A., Steltzner, A. D., San Martin, A. M., Burkhart, P. D., and Mendeck, G. F., "Mars Science Laboratory: Entry, Descent, and Landing System Performance," IEEAC Paper 1467, March 2006.

R. Cummings
Associate Editor